

## VALIDATION OF LES PREDICTIONS FOR TURBULENT FLOW IN A CONFINED IMPINGING JET REACTOR

Matteo ICARDI<sup>1\*</sup>, Emanuela GAVI<sup>2</sup>, Daniele L. MARCHISIO<sup>1</sup>,  
Michael G. OLSEN<sup>2</sup>, Rodney O. FOX<sup>2</sup> and Djamel LAKEHAL<sup>3</sup>

<sup>1</sup> Dip. Scienza dei Materiali e Ingegneria Chimica, Politecnico di Torino, Torino, Italy

<sup>2</sup> Iowa State University, Ames, USA

<sup>3</sup> ASCOMP GmbH, Zurich, Switzerland

\*Corresponding author, E-mail address: matteo.icardi@polito.it

### ABSTRACT

This work focuses on the prediction of turbulent flow in a Confined Impinging Jet Reactor using Large Eddy Simulation (LES). Three dimensional transient simulations were performed for various flow rates, ranging from quasi-steady laminar flow to unsteady turbulent flow. Predictions of the mean and fluctuating velocities were compared with micro Particle Image Velocimetry (mPIV) data. Good agreement was found both for the mean velocity components and the fluctuations. The study highlights the importance of properly imposing the inflow boundary conditions to mimic the pumping instability, without which the CFD model does not reproduce the correct unsteady flow behavior. As the Reynolds number range was still low to moderate, the sub-grid scale modeling was not an issue here and the small scales were of less importance, as long as scalar transport and chemical reaction are not in play. An important finding is the good prediction of the high velocity fluctuations due to the natural instability of the system strongly enforced by the jets asymmetry and unsteadiness.

### NOMENCLATURE

$p$	pressure
$\mathbf{u}$	velocity
$\rho$	density
$\nu$	kinematic viscosity
$\eta$	Kolmogorov micro-scale length
$\tau_j$	reactor mean residence time

### INTRODUCTION

In many chemical/process engineering fields (e.g., pharmaceutical, cosmetics, pesticides, etc.) there is a strong interest in micro- and nano-particles that can be produced by precipitation in particular types of micro-mixers, such as the Confined Impinging Jet Reactor (CIJR). CIJRs are indeed widely used nowadays due to their high mixing efficiency. But to achieve the best efficiency, these systems are still under severe design conditions to control and optimize important properties of the nano-particle, namely the Particle Size Distribution (PSD), the particle shape and morphology, as well as the particle composition. PSD is indeed strongly dependent on

the mixing rate, and very fine particles with very narrow distributions are obtained only under extremely efficient mixing conditions. It has become clear that optimum design conditions can conveniently be obtained by the aid of an advanced Computational Fluid Dynamics (CFD) model.

It is in this spirit that the present work has been undertaken. We present here recent predictions of the flow field for a non-reactive test-case, compared to mPIV measurements of Gavi (2009). The objective is to first validate the computational tool chosen to predict the fluid dynamics in the reactor, before developing - in a later stage - adequate models to account for reactivity of the system. For this purpose, the influence of grid resolution, boundary conditions and turbulence modeling are all analyzed and discussed. In Sec. 1 we briefly present the theoretical background and concepts of turbulent flow simulation, while numerical methods and operating conditions are described in Secs. 2 and 3. The results are then discussed and compared with the available experimental data.

### MODEL DESCRIPTION

#### Fluid flow equations

The single phase incompressible flow inside the CIJR is investigated in this work by solving the incompressible Navier-Stokes equations:

$$\nabla \cdot \mathbf{u} = 0, \quad (1)$$
$$\rho \left( \frac{\partial \mathbf{u}}{\partial t} + \mathbf{u} \cdot \nabla \mathbf{u} \right) = -\nabla p + \nu \Delta \mathbf{u}. \quad (2)$$

The ideal method to solve these equations depends on the flow conditions, i.e. the Reynolds number  $Re$ . In these flows, however, although the inflow conditions are those characteristic of a laminar flow (low  $Re$ ), the jets impingement creates strong flow instabilities and spatial variations that lead to turbulence (i.e. containing a wide range of time and length scales). So if the grid is not fine enough to resolve all the scales arising from the interaction of the jets, a model is required to represent their effect on the macro-scale flow. This becomes then a 'turbulent modeling problem'.

For turbulent flows the system of equations (1-2) are solved either within the Reynolds-Averaged Navier-Stokes (RANS) framework or in a filtered form (Large

Eddy Simulation, LES), where flow variables appear now as filtered quantities

$$\bar{\mathbf{u}} = \int G(\mathbf{r}, \mathbf{x}) \mathbf{u}(\mathbf{x} - \mathbf{r}, t) d\mathbf{r}, \quad (3)$$

and  $G$  is the convolution function, which depends on the simulation platform. The most common one is the so-called ‘‘box filter’’, which directly makes use of the finite volumes approximation of the spatial operators. The application of Eq. (3) to the above system of equations results in a closure problem, namely the residual stress terms

$$\tau_{ij} = \overline{u_i u_j} - \overline{u_i} \overline{u_j}. \quad (4)$$

need to be modeled by using a so-called sub-grid scale (SGS) model, which uses macro-scale flow variables.

On the other hand, if the grid is dense enough to resolve all the length-scales of the flow until the Kolmogorov micro-scale (or the Batchelor micro-scale in the case of chemically reacting flows), we are performing a Direct Numerical Simulation (DNS). However, for the DNS to be accurate, the algorithmics must be accurate enough to avoid numerical diffusion, which can actually play the role of a filter ‘artificially introduced’ by discretization errors.

In this work both LES and DNS have been carried out and predictions at different Reynolds numbers have been validated via comparison with experimental data. The flow has been simulated under fixed and variable inflow conditions, on which flow unsteadiness actually depends.

#### Reactor geometry

Figure 1 represents the  $x/y$  plane of the three-dimensional geometry of the CIJR used both for simulations and experiments. The flow comes from two opposing tubes in the upper part of the reactor where the jets collide forming complicated structures and then exit through the lower part. The flow regime in the reactor can be characterized by the jet Reynolds number, defined based on inlet jet diameter and average inflow velocity.

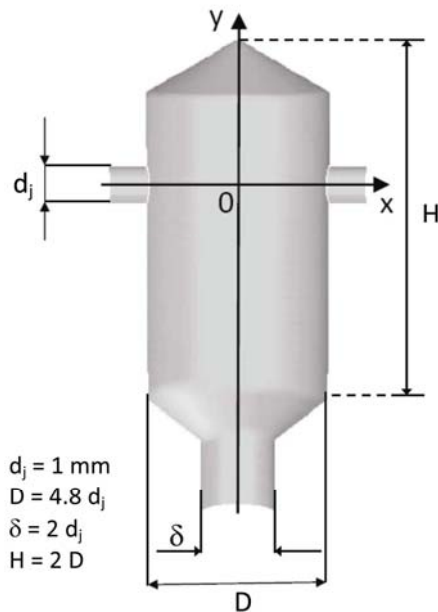


**Figure 1** Schematic geometry of the CIJR under study.

## NUMERICAL METHODS

Computations are carried out with the commercial Computational Multi-Fluid Dynamics (CMFD) code TransAT<sup>1</sup>. The equations are solved with a finite volume approximation, where the pressure-velocity coupling is performed by using the SIMPLEC algorithm. Time discretization is performed with a 3<sup>rd</sup> order explicit Runge-Kutta scheme (for LES) or a 2<sup>nd</sup> order implicit scheme in time (for DNS). The advective terms are discretized with the HPLA scheme (Zhu, 1991), which combines a second-order upstream-weighted approximation with the first-order upwind differencing under the control of a convection boundedness criterion. Although there are other schemes more suitable for DNS and LES, which give less numerical diffusion, HPLA assures a better convergence and stability. Furthermore a test simulation with QUICK scheme was performed revealing no significant differences.

Solid boundaries of the reactor are represented with the Immersed Surface Technique (IST) in which the cells near the walls are marked using a signed distance function (known as the solid level-set function) and treated in a separate way to impose no-slip condition there. Since the walls are immersed in a Cartesian grid, meshing time is considerably reduced and the higher accuracy of the numerical scheme can be preserved since the grid-skewness induced diffusion is simply eliminated. These two elements make the IST approach very useful to conduct unsteady turbulent flows in complex geometries.

While for DNS no modeling assumption is made, for LES the Smagorinsky SGS model has been used with a model constant  $C_s=0.08$  to limit diffusion in the near-wall region. In the wall flow-regions in question, the Werner-Wengle wall functions (1/7<sup>th</sup> power-law, Werner and Wengle 1989) are used, together with the van Driest damping function (van Driest 1956).

## OPERATING CONDITIONS AND NUMERICAL DETAILS

Fluid properties are selected by reference to the experiments, which employed an aqueous solution of urea with a density  $\rho=1.141 \text{ g/cm}^3$  and a viscosity  $\mu=1.914 \text{ cPs}$ . Four different inlet flow rates ( $FR$ ) are imposed: 10, 20, 40 and 90 mL/min. The Reynolds numbers calculated using the inlet diameters and the mean velocities show that the flow regime in the inlet tubes is laminar, thus parabolic velocity profiles have been imposed at the inlet.

The first set of simulations has been performed with inflow velocities calculated theoretically from the nominal flow rates imposed by the pumps (Table 1).

$FR$ , ml/min	Mean inlet velocity, m/s	$\tau$ , s	$Re$	$\eta$ , $\mu\text{m}$
10	0.106	1.04	63	45
20	0.212	0.52	126	27
40	0.424	0.26	253	16
90	0.955	0.115	569	9

**Table 1** Nominal flow rates, mean velocities, mean residence times, jet Reynolds numbers and Kolmogorov micro-scale length.

<sup>1</sup> TransAT is a product of ASCOMP GmbH (www.ascomp.ch)

An initial set of simulations has been carried out with four different grids comparing LES (performed using coarser grids) with DNS (finer grids). Details about the different grids (within the IST context) are reported in Table 2. Simulations were performed on a Linux cluster with either a shared or a distributed memory parallelism. The former has single-block grids (Open-MP library), and the latter has multi-block grids (MPI library).

Dimensional analysis and grid sensitivity studies revealed that for the two lowest  $FR$ , even with the coarse grids, all the scales can be solved and the LES can be considered as DNS. In this case in fact the flow is still laminar. With the two highest  $FR$  instead, the SGS model starts to become important but no significant differences between LES and DNS were found, proving that the SGS model is accurately describing the unresolved scales. Thus the results discussed later are the ones computed on the coarse grid.

#	# of cells per block	# blocks	Internal cells	$\Delta x$ , $\mu\text{m}$	Parallel
1	68x60x128	1	$3.5 \cdot 10^5$	50-80	O-MP
2	100x84x150	1	$8.5 \cdot 10^5$	30-60	O-MP
3	46x42x34	36	$8 \cdot 10^5$	50-60	MPI
4	82x52x66	36	$8 \cdot 10^6$	17-25	MPI

**Table 2** Computational grids used for grid convergence analysis and DNS/LES comparison.

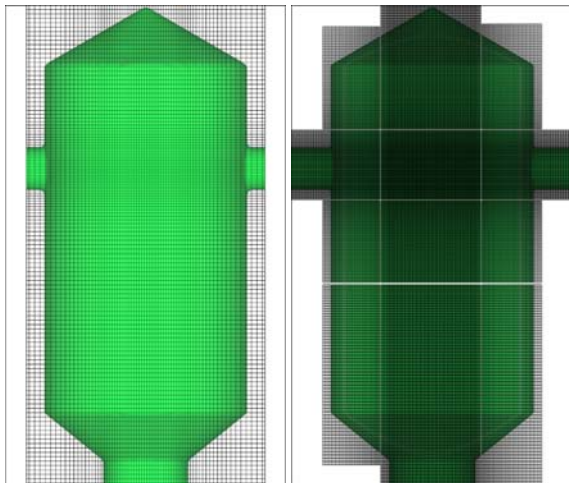


**Figure 2** The coarse single-block grid (n.1) used for simulations and the finest multi-block one (n.4).

Additional mPIV data in a region very close to the inlets ( $x = \pm 2$  mm) were also analyzed and they appeared to be different from the nominal ones. Further, looking at the inflow statistics of the jets, a strong unsteadiness and asymmetry was found. This observation suggests that the experiments were not conducted with perfectly symmetrical and steady inflows. Consequently, a second set of simulations has been performed using unsteady asymmetric mean inflow velocities, as reported in Table 3.

Left Mean	Left St. Dev	Right Mean	Right St. Dev
0.139 m/s	0.008 m/s	0.132 m/s	0.009 m/s
0.347 m/s	0.007 m/s	0.275 m/s	0.014 m/s
0.570 m/s	0.107 m/s	0.667 m/s	0.040 m/s
1.20 m/s	0.203 m/s	1.13 m/s	0.273 m/s

**Table 3** Mean values and standard deviations of the  $x$ -velocity in the inflow regions near the inlets.

The frequency spectra of the experimental velocities near the inlets were analyzed. The main oscillating frequency was identified, and found to be similar in both the left and right inflow streams, estimated to be approximately  $1,6 \text{ s}^{-1}$  for the lowest flow rate. Since this peak could not be clearly identifiable for higher flow rates (because the mPIV sampling frequency of  $4 \text{ s}^{-1}$  does not allow capturing frequencies higher than  $2 \text{ s}^{-1}$ ) we decided to set them proportional to the nominal flow rates.

Therefore in the present simulations the oscillating inflows, solely determined by the experimental data, were imposed by using a single harmonic oscillation in both the inflows. They were set to be in phase opposition in order to emphasize the effects of unsteady asymmetric flows. The oscillation amplitude was then set proportional to the original parabolic profile (to avoid a negative inflow velocity) with a factor of 0.1 that fits the standard deviation obtained in the experiment with  $FR = 10 \text{ mL/min}$ , which is the case where the external instabilities are more evident.

## RESULTS

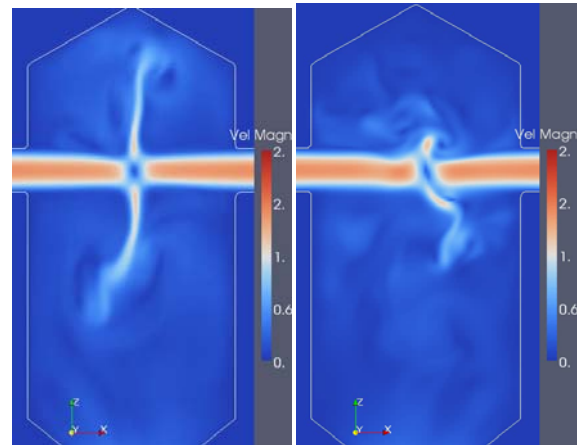


**Figure 3** Instantaneous velocity magnitudes with 90 ml/min flow rate and constant symmetric inflows.

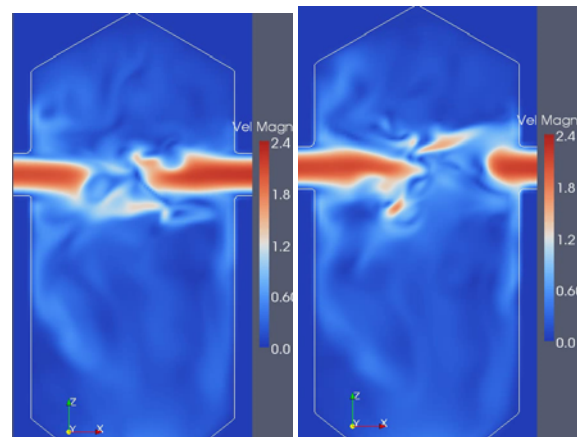


**Figure 4** Instantaneous velocity magnitudes with 90 ml/min flow rate and oscillating asymmetric inflows.

Simulations are analyzed after the transient effects due down, so that the influence of the initial condition had disappeared (between  $t=4\tau$  and  $t=8\tau$ ). Figure 3 and

Figure 4 represent two instantaneous velocity magnitude fields with  $FR = 90 \text{ mL/min}$  and different inflow conditions. The former shows a quasi-steady behavior with large-scale fluctuations. In the latter, the variable asymmetric inflow conditions drastically change the flow behavior, developing of more scales, which are not created with constant inflows, even after refining the grid. These different scales are clearly identifiable when looking at the vorticity magnitude in *Figure 5* and *Figure 6*.

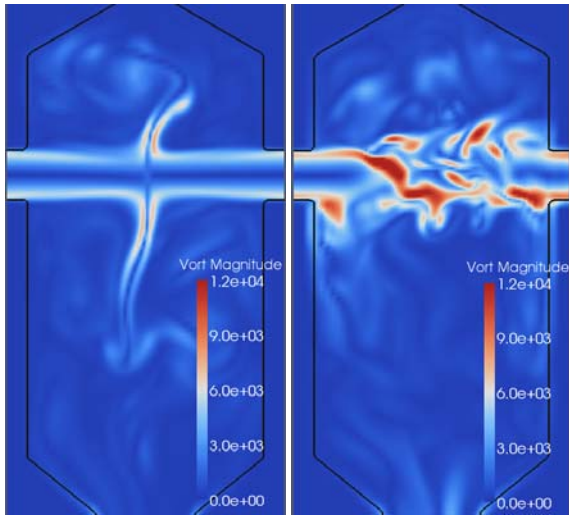


**Figure 5** Instantaneous vorticity magnitudes in the reactor. Comparison between constant inflows (left) and unsteady asymmetric inflows (right).

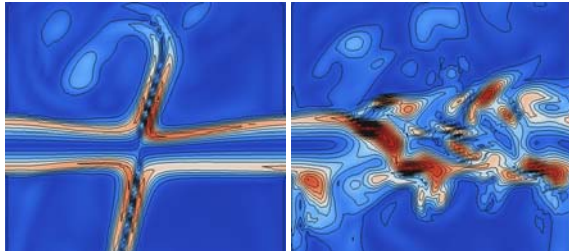


**Figure 6** Details of instantaneous vorticity magnitudes in the center of the reactor. Comparison between constant inflows (left) and unsteady asymmetric inflows (right).

Vorticity is a good indicator of the flow structures and scales created/dissipated and their interaction with the local shear. The left panels in *Figure 5* and *Figure 6*, taken from the constant inflow simulation, show the onset of large structures created at impingement. The right panels, taken from the variable inflows simulation, reveal the existence of smaller scales, generated from the breakup of the larger ones, responsible for the dissipation mechanism of turbulence. It is this process of creation/destruction of flow scales followed by small-scale vorticity generation which is important for phenomena like mixing, entrainment, and scalar diffusion mechanisms.

Comparisons with experiments can be made by analyzing the statistics of the flow along the inlet and outlet axes near the impinging point. This is in fact the region where the most important phenomena occur. *Figure 7* and *Figure 8* show for the lowest  $FR$  the mean and root-mean-square (RMS) axial velocity profiles, respectively. DNS and LES are compared with the experiments for both

constant and oscillating inflows. As we already pointed out, especially for this flow rate, DNS and LES results are very similar and the two lines are often overlapped. When using constant inflows the simulation reaches a steady state in a short time. Although the mean velocity profile is close to the experiments the fluctuations are totally absent with constant inflows. With unsteady inflows the model is capable of better predicting both the mean and the fluctuations, as compared to the experimental data. The same is true for the  $y$ -velocity profile reported in *Figure 9* and *Figure 10* for the same flow rate ( $FR = 10 \text{ mL/min}$ ). It can be observed that the induced instability reduces the longitudinal velocities and that the impingement point is no longer stable.

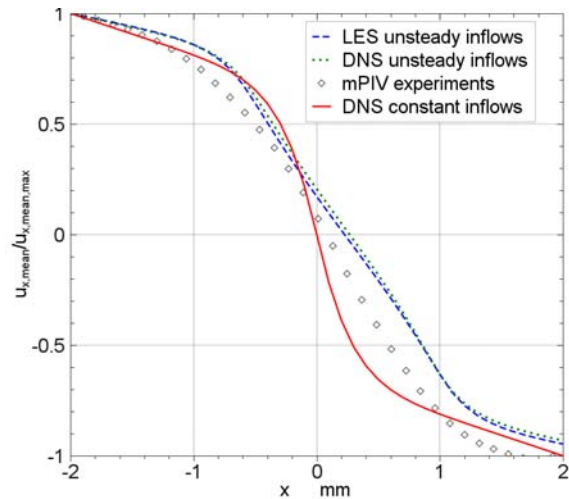


**Figure 7** Mean axial velocity along the  $x$ -axis at  $y = 5.6 \text{ mm}$  with  $FR = 10 \text{ mL/min}$ . Comparison between LES and DNS with unsteady inflows, mPIV experiments and DNS with constant inflows.

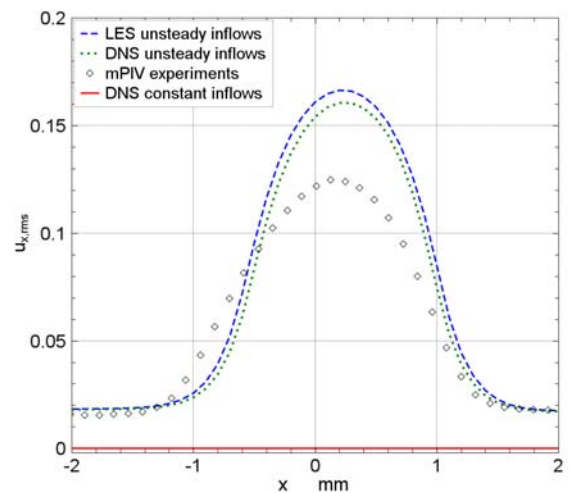


**Figure 8** Rms of axial velocity fluctuations along the  $x$ -axis at  $y=5.6 \text{ mm}$  with  $FR = 10 \text{ mL/min}$ . Comparison between LES and DNS with unsteady inflows, mPIV experiments and DNS with constant inflows.

Increasing the inflow velocity triggers the onset of an unsteady flow regime, and a weakly turbulent behavior can be observed. In particular with intermediate flow rates ( $FR = 20\text{-}40 \text{ mL/min}$ ) the flow starts to oscillate even with

constant inflow but the amplitude and positions of oscillations are better predicted with the oscillating boundary conditions.

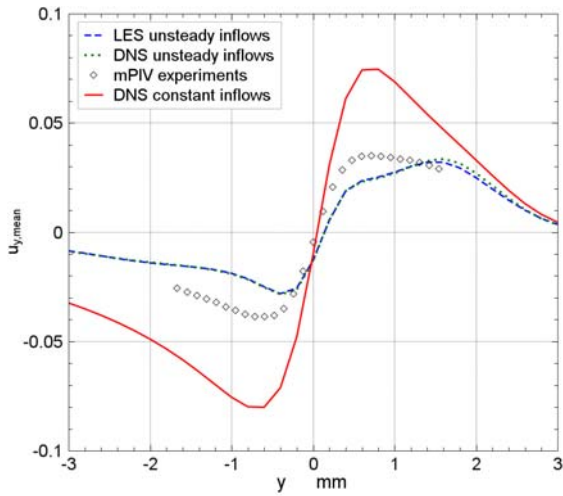


**Figure 9** Mean-longitudinal velocity along the y-axis at  $x = 0$  mm with  $FR = 10$  ml/min. Comparison between LES and DNS with unsteady inflows, mPIV experiments and DNS with constant inflows.

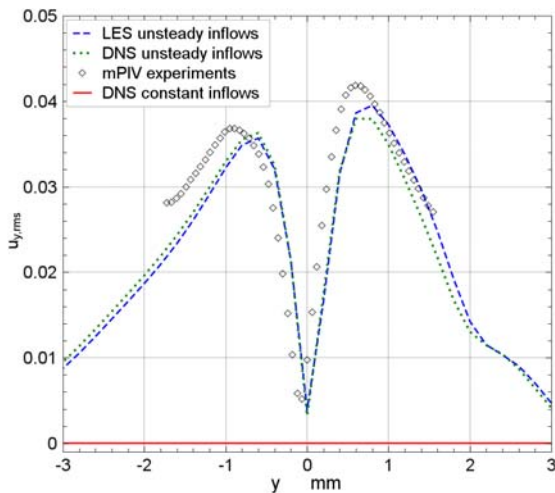


**Figure 10** Rms of longitudinal velocity fluctuations along the y-axis at  $x = 0$  mm with  $FR = 10$  ml/min. Comparison between LES and DNS with unsteady inflows, mPIV experiments and DNS with constant inflows.

Further interesting comments can be made analyzing the case with  $FR = 90$  mL/min. In Figure 11 and Figure 12 the axial velocity statistics for this flow rate are compared to experimental data for DNS and LES with constant and unsteady inflows. Both the mean and the fluctuations show a significant improvement when employing the unsteady boundary conditions. These boundary conditions can predict the relatively high fluctuations along the entire axes. However, looking at points  $x=2$  mm and  $-2$  mm the fluctuations seem to be too asymmetric, probably because the assumption of phase opposition used for the inflows is too strong and causes the impingement point to be more shifted to the right than in the experiments. This shifting is further confirmed in the mean velocity profile and in Figure 13 and Figure 14, which depict the y-velocity

statistics. As we notice for the lowest flow rate, the longitudinal mean velocities and fluctuations in the center line  $x = 0$  are smaller when the impingement point is unstable.

It is important to notice that when comparing velocity fluctuations obtained from mPIV and DNS/LES it is necessary to account for the difference in resolution between experiments and simulations. In fact since the mPIV measurement volume is  $140 \mu\text{m}$ , the smallest scales of turbulence may not be detected and part of the turbulent energy, especially at high  $Re$ , may not be measured in experiments. This difference in resolution may have contributed to the difference in magnitude between the measured and predicted velocity fluctuations.

As reported in the previous section, also DNS results revealed the same influence of the boundary conditions. In fact, for the considered flow regimes, the turbulent behavior of the system is not due only from the jets impingement but also from inlet instability and using constant inflows, even the DNS shows a strongly unsteady behavior limited to a small region in the center of the reactor in contrast to the experiments. This suggests that, although the results are very close to the experimental data, the remaining mismatches of the CFD model are not coming from an inadequate turbulence model or grid resolution, but they could come from the approximation of the boundary conditions. To increase their accuracy, more frequencies could be introduced in the oscillations and more detailed mPIV measurements near the inlets could be analyzed.

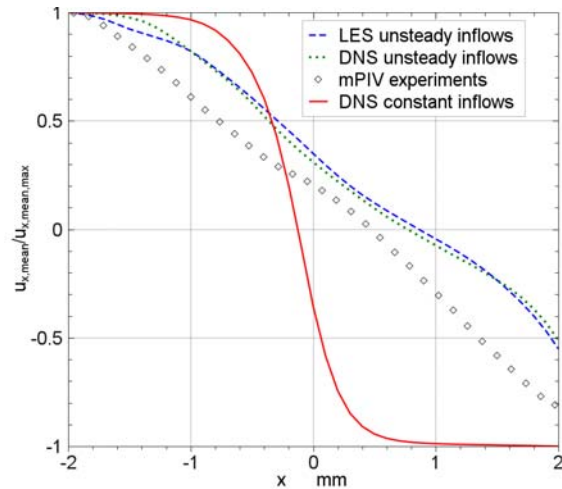


**Figure 11** Mean axial velocity along the x-axis at  $y=5.6$ mm with  $FR = 90$  ml/min. Comparison between LES and DNS with unsteady inflows, mPIV experiments and DNS with constant inflows.

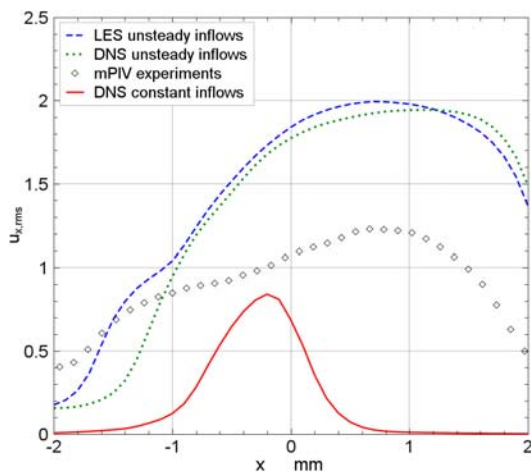


**Figure 12** Rms of axial velocity fluctuations along the x-axis at  $y = 5.6$  mm with  $FR = 90$  ml/min. Comparison between LES and DNS with unsteady inflows, mPIV experiments and DNS with constant inflows.

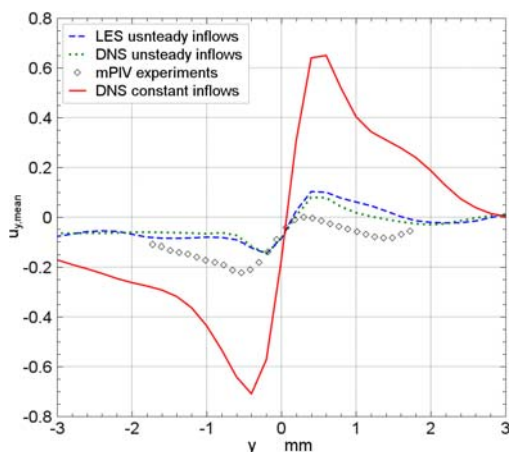


**Figure 13** Mean longitudinal velocity along the y-axis at  $x = 0$  mm with  $FR = 90$  ml/min. Comparison between LES and DNS with unsteady inflows, mPIV experiments and DNS with constant inflows.

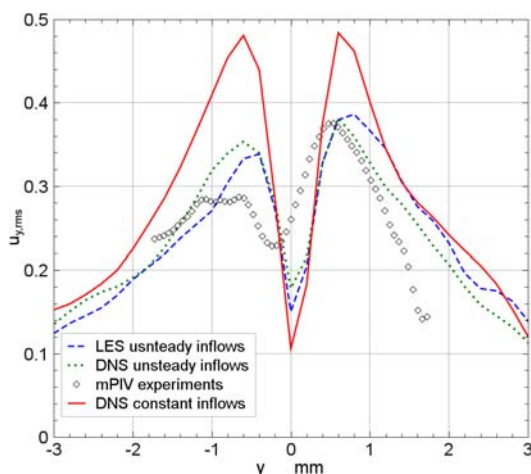


**Figure 14** Rms of longitudinal velocity fluctuations along the y-axis at  $x=0$  with  $FR = 90$  ml/min. Comparison between LES and DNS with unsteady inflows, mPIV experiments and DNS with constant inflows.

However, an intriguing fact is that these results corroborate well with the experiments and suggest that the natural instability of the flow observed in DNS with constant inflows is not sufficient to explain the turbulent behavior observed which could be induced by oscillations in the boundary conditions. To go into more depth we performed a simulation imposing a fixed pressure at the inlet pipes (estimated with the previous simulations to have the same mean inflow velocity) but even in this case we obtained results very similar to the constant velocity ones.

In summary, most of the unsteadiness and inhomogeneity observed in the CIJR are clearly due to the variable inflow conditions, causing higher mixing and momentum exchange (and eventually scalar transport). It is obvious that one should be cautious in advancing such an explanation, but the lack of analytical investigation related to impinging-jet instabilities may plead in favor of our arguments.

## CONCLUSION

This work demonstrates the importance of properly imposing the inflow boundary conditions when the flow is solved within both the LES and DNS contexts. In fact, as shown experimentally by Gavi (2009), RANS simulations with constant inflow profiles give in some situations good agreement between CFD and experiments, because time averaging is implicitly taken into account in the equations. Instead if a more precise description of the unsteady flow field is required, LES and DNS simulations can be performed but they must be provided with more accurate boundary conditions to reproduce experiments. Starting from the present results, the computational model will be extended to consider reactive processes, including turbulent precipitation and reactions in the CIJR.

## ACKNOWLEDGEMENTS

Thanks to the ASCOMP support crew (D. Caviezel and C. Narayanan) who helped set up this problem.

## REFERENCES

- GAVI, E., (2009), "Investigation of turbulent precipitation of nanoparticles in a Confined Impinging Jets Reactor", *Ph.D. Thesis*, Politecnico di Torino, Italy.
- GAVI, E., MARCHISIO, D.L. and BARRESI, A., (2006), "CFD modeling and scale-up of Confined Impinging Jet Reactors", *Chem. Eng. Sci.*, 62, 2228-2241.
- MARCHISIO, D.L. (2009), "Large Eddy Simulations of mixing and reaction in a Confined Impinging Jet Reactor", *Comp. Chem. Eng.*, 33, 408-420.
- LIU, Y, OLSEN, M.G. and FOX, R.O. (2009), "Turbulence in a micro-scale planar confined impinging-jets reactor", *Lab on a Chip*, 9, 110-1118.
- FOX, R.O., (2003), "Computational Models for Turbulent Reacting Flows", *Cambridge University Press*, Cambridge.
- FERZIGER, J. and PERIC, M., (1997), "Computational Methods for Fluid Dynamics", *Springer Verlag*, Berlin.
- POPE, S.B., (2005), "Turbulent Flows", *Cambridge University Press*, Cambridge.
- SCHWERTFIRM, F. et al. (2007), "The Low Reynolds number turbulent flow and mixing in a confined impinging jet reactor", *Int. J. Heat and Fluid Flow*, 28, 1429-1442.

JOHNSON, B. and PRUD'HOMME, R., (2003), "Chemical processing and micro-mixing in confined impinging jets", *AIChE J.*, 49, 2264-2282.

JOHANSONN, P. and ANDERSSON, H., (2005), "Direct Numerical Simulation of two opposite wall jets", *Phys. Fluids* 17 (5).

ASCOMP GmbH, (2009), "Multi-fluid Navier-Stokes Solver TransAT User Manual".

ZHU, J, (1991), "A low diffusive and oscillation free convection scheme", *Commun. Appl. Num. Methods*, 7, 225-232.

VAN DRIEST, E. R., (1956), "On turbulent flow near a wall", *J. Aerospace Sci.*, 23, 1007-1011.

WERNER, H. and WENGLER, H., (1989), "Large-eddy simulation of the flow over a square rib in a channel", in *Proc. Seventh Symp. Turbulent Shear Flows*, 10.2.1-10.2.6.